

Superstoichiometric Alloying of H and Close-Packed FeNi under High Pressures: Implications for Hydrogen Storage in Planetary Cores

Helene Piet

Arizona State University <https://orcid.org/0000-0003-3152-0132>

Andrew Chizmeshya

Arizona State University

Bin Chen

University of Hawaii at Manoa

Stella Chariton

University of Chicago

Eran Greenberg

University of Chicago

Vitali Prakapenka

University of Chicago <https://orcid.org/0000-0001-9270-2330>

Peter Buseck

Arizona State University

Sang-Heon Shim (✉ sshim5@asu.edu)

Arizona State University

Article

Keywords: Superstoichiometric Close-packed Alloys, Polyhydrides, Mass-radius Relations, Massive Exoplanets

Posted Date: November 19th, 2020

DOI: <https://doi.org/10.21203/rs.3.rs-103113/v1>

License: © ⓘ This work is licensed under a Creative Commons Attribution 4.0 International License.

[Read Full License](#)

1 Superstoichiometric Alloying of H and Close-Packed
2 FeNi under High Pressures: Implications for Hydrogen
3 Storage in Planetary Cores

4 H. Piet^{1*}, A. V. G. Chizmeshya², B. Chen³, S. Chariton⁴,
E. Greenberg⁵, V. B. Prakapenka⁴, P. R. Buseck^{1,2}, S.-H. Shim^{1*}

¹ School of Earth and Space Exploration, Arizona State University, Tempe, Arizona, USA.

² School of Molecular Sciences, Arizona State University, Tempe, Arizona, USA.

³ Hawaii Institute of Geophysics and Planetology, University of Hawaii at Manoa, Honolulu, Hawaii, USA.

⁴ Center for Advanced Radiation Sources, University of Chicago, Chicago, Illinois, USA.

⁵ Now at Soreq Nuclear Research Center, Applied Physics Department, Yavne, Israel.

* To whom correspondence should be addressed; E-mail: helene.piet@asu.edu, shdshim@asu.edu.

5 November 4, 2020

6 **Abstract**

7 Although high pressure promotes alloying between hydrogen and iron, it has been believed
8 that H/Fe is limited to 1 in the close-packed alloys. We report a substantial increase in the H
9 solubility for iron through stabilization of superstoichiometric close-packed alloys promoted by
10 Ni and high temperature. We also observe Fe-H polyhydrides at temperatures over 2500 K at
11 high pressures, stability of which has been unknown at temperatures relevant for the planetary
12 interiors. Considering recent results, large storage of H in the planetary cores is possible from

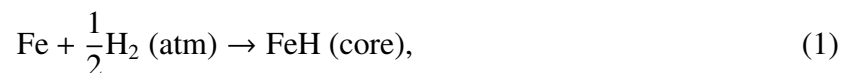
13 H₂-rich to even H₂O-rich conditions. The H storage in the core can change the mass-radius
14 relations where H has been assumed to de-gas to the atmosphere. Such H solubility and
15 storage in the core are important to consider for understanding the “diluted core” of Jupiter, the
16 “radius cliff” in the sub-Neptune exoplanets population, and massive exoplanets with very thin
17 atmospheres.

18 Introduction

19 Based on geochemical and geophysical evidence, Earth’s core is primarily composed of FeNi alloyed
20 with a considerable amount of light elements to explain its observed density deficit¹. Candidate
21 elements are silicon, sulfur, oxygen, carbon and hydrogen². Despite its dominance in planetary
22 systems, the effects of hydrogen are not well understood relative to other light elements because of
23 experimental challenges associated with its study at high pressure–temperature (P – T) conditions.
24 Thanks to recent technical advances^{3,4}, and an evolving vision of the important role of hydrogen
25 in the dynamics and compositions of the interiors of a wide range of planets⁵, the last decade has
26 seen a surge in studies of the Fe–H system under high P – T conditions^{6–12}. Some of these studies
27 have documented the stability of face-centered cubic structured (fcc) FeH_x at 10–137 GPa^{6,10,12}.
28 However, in these studies, it appears that molar H/Fe for the close-packed alloy (i.e., H solubility in
29 fcc- FeH_x) is limited to ≈ 1 (or $x \leq 1$).

30 Recently, a series of polyhydrides have been described in which H/Fe increases with increasing
31 pressure: FeH_2 at 67 GPa, FeH_3 at 86 GPa, and FeH_5 at ≥ 130 GPa^{7,8}. This discovery sparked
32 an interest in the domain of superconductivity, where highly hydrogenated compounds such as
33 H_3S and LaH_{10} have shown record high critical temperatures^{13,14}. The results are also potentially
34 important for the interiors of hydrogen-rich planets, such as gas giant planets and sub-Neptune
35 exoplanets. Data from the Juno mission¹⁵ has stirred our conventional view of the internal structure
36 of hydrogen-rich gas giants such as Jupiter, where instead of a sharp hydrogen-core interface,
37 the gravitational data suggests a compositional gradient over a large depth range in the interior.
38 However, the polyhydrides^{7,8} were all synthesized at temperatures much lower (500–1500 K) than
39 those expected for planetary interiors (over a few thousand kelvins) and some theoretical studies
40 still predict the close-packed structured Fe–H alloys as the most stable form up to 400 GPa¹⁶.

41 In the magma ocean of a planet surrounded by a hydrogen-rich atmosphere (atm), Fe–H alloys
42 would form under reducing conditions at low pressures¹⁷:

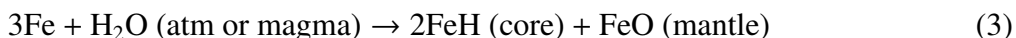


43 which would facilitate large hydrogen storage into the core. It has been believed that water-rich
44 magma oceans would oxidize iron metal into iron oxides and release hydrogen to the atmosphere¹⁸:

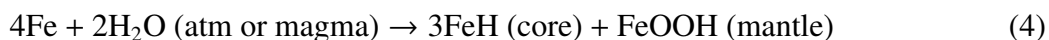


46 This reaction consumes metallic iron and converts it to a component incorporated into the mantle.
47 Therefore, if occurs, the reaction would result in a reduction of the size of the metal core while the
48 mantle becomes enriched with FeO. Even a coreless planet has been discussed as an end member
49 case under extreme water-rich conditions¹⁸.

50 However, recent high-pressure experiments have shown the formation of FeH_x alloys when iron
51 metal reacts with H₂O, where:



52 at 6–84 GPa¹⁹ and:



53 at >78 GPa²⁰. These reactions indicate that core formation would be inevitable, even under H₂O
54 rich conditions. These reactions also suggest that a large amount of hydrogen can efficiently be
55 stored in the core and contributions from hydrogen outgassing to form an H-rich atmosphere would
56 be limited to very low-pressure regimes.

57 Earth's core contains some Ni (5.5 wt.%,²¹) and Ni may affect the solubility of light elements
58 in the core²². However, potential effects of Ni on the solubility of H in the core have seldom been
59 studied and the existing data are limited to ≤15 GPa and 1673 K²³. Here, we study the effect of Ni
60 on the solubility of hydrogen in metallic iron formed at pressures and temperatures up to 77 GPa
61 and 2790 K in the laser-heated diamond anvil cell (LHDAC). Our experimental results indicate that
62 Ni and high temperatures stabilize the close-packed structured (in this case face-centered cubic, fcc)

63 phase over polyhydrides with direct H-to-H bonding, and promotes the solubility of H in fcc Fe
64 beyond the level previously known^{6,10,12}. A dramatic increase of H storage in the metallic core of a
65 planet can alter the mass-radius relations for planets composed of hydrogen and metallic Fe because
66 the H atoms would be much more densely packed at the pressures expected for such a core. It is
67 therefore important to consider the consequences of Fe-H alloying for understanding the formation
68 and the evolution of H-rich atmospheres of gas giant and sub-Neptune planets.

69 **Results and discussion**

70 **In situ X-ray diffraction experiments**

71 We performed synchrotron X-ray diffraction (XRD) experiments for the Fe-H and the Fe-Ni-H sys-
72 tems at 26–89 GPa and 1170–2840 K in laser-heated diamond-anvil cells. Important improvements
73 made in this study include: (i) heating H-rich samples to temperatures sufficient for planetary appli-
74 cations by taking advantage of pulsed laser heating³, and (ii) in-situ X-ray diffraction measurements
75 during heating of H-rich samples to monitor chemical reactions⁴.

76 At pressures below 30 GPa, our results for the Fe-H system are largely consistent with previous
77 reports^{6,7,10,17}: (i) formation of dhcp-FeH (dhcp: double hexagonal close packed) by compression of
78 metallic Fe in a H medium at 300 K^{7,17}, and (ii) formation of fcc-FeH upon heating to temperatures
79 above 1160 K. At 66 GPa and 2140 K, dhcp-FeH_x converts to tetragonal-FeH₂ (space group:
80 *I4/mmm*). At 89 GPa, our in situ diffraction patterns show that dhcp-FeH_x converts to a tetragonal-
81 FeH₂ + cubic-FeH₃ (space group: *Pm $\bar{3}$ m*) mixture at 1890 K. Upon further heating, however, the
82 cubic phase disappears and the sample converts to single tetragonal-FeH₂ at 2690 K (Fig. 1). These
83 observations agree with previous reports on polyhydrides where the high-temperature stability of
84 polyhydrides were inferred from XRD patterns measured after temperature quench from heating
85 at ≤ 1500 K⁷. Here, we extend the temperature range and provide direct evidence for the stability
86 of tetragonal-FeH₂ up to 2470 K at 66 GPa and 2690 K at 89 GPa (Fig. 1A), and for FeH₃ up to
87 2540 K at 89 GPa. To our knowledge, this is the first direct evidence measured at in-situ high

88 temperatures for the relevance of polyhydrides to the interiors of hydrogen-rich planets. We also
89 note the presence of fcc-FeH after temperature quench at 89 GPa, which is discussed below.

90 While enabling heating of the samples in a H medium to very high temperatures, a pulse
91 heating run involves with integration of thousands of short heating events^{3,4}. Despite the difference
92 in time duration and heating style, as discussed above, the phase behavior of the Fe-H system
93 agrees well with those previously reported with different heating methods at the overlapping
94 P - T ranges^{6,10,12}. As previously documented, we found that the reaction between iron metal and
95 hydrogen is spontaneous and therefore the kinetic effects are negligible. In fact, iron metal reacts
96 with hydrogen even without heating in our experiments, also consistent with previous reports¹⁷.

97 We conducted similar experiments for the Fe-Ni-H system. Before heating at 33 GPa, Fe-
98 6.5(4)%Ni fully reacts with hydrogen to form a dhcp phase, similar to the behavior of the Fe-H
99 system. However, unlike the Ni-free system, the fcc phase does not appear during heating, and
100 dhcp-FeNiH remains stable up to 2790 K at this pressure. At 77 GPa and 1880 K, however, dhcp is
101 converted to fcc and tetragonal-FeNiH₂ phases, where fcc is the dominant phase. At 2720 K, the
102 tetragonal-FeNiH₂ phase disappears, with only the fcc phase present in the pattern (Figs 1A and B).
103 These results clearly indicate the significant effects of Ni on stable crystal structures in the Fe-H
104 system at high P - T .

105 After laser heating at 33 GPa, the measured unit-cell volume of dhcp-FeNiH agrees with its
106 Ni-free counterpart (dhcp-FeH) at the same pressure condition. We interpret that Ni does not
107 significantly affect the unit-cell volume of the Fe-H alloy phase, similar to the case of Fe-Ni alloy
108 with low Ni content²⁴. The unit-cell volume of fcc-FeH_{*x*} measured after synthesis at 26 GPa also
109 agrees with previous reports at this pressure range^{6,10,12}. We also found that the tetragonal-FeNiH₂
110 phase synthesized at 77 GPa has a similar unit-cell volume to that of tetragonal-FeH₂⁷ (the data
111 will be reported elsewhere).

112 Above 30 GPa, however, the unit-cell volumes of both fcc-FeH_{*x*} and fcc-FeNiH_{*x*} are greater than
113 reported for fcc-FeH_{*x*}^{6,10,12}, suggesting more H in the crystal structure (Fig. 2A and Table S1). In
114 particular, both fcc-FeH_{*x*} and fcc-FeNiH_{*x*} synthesized above 70 GPa show larger unit-cell volumes

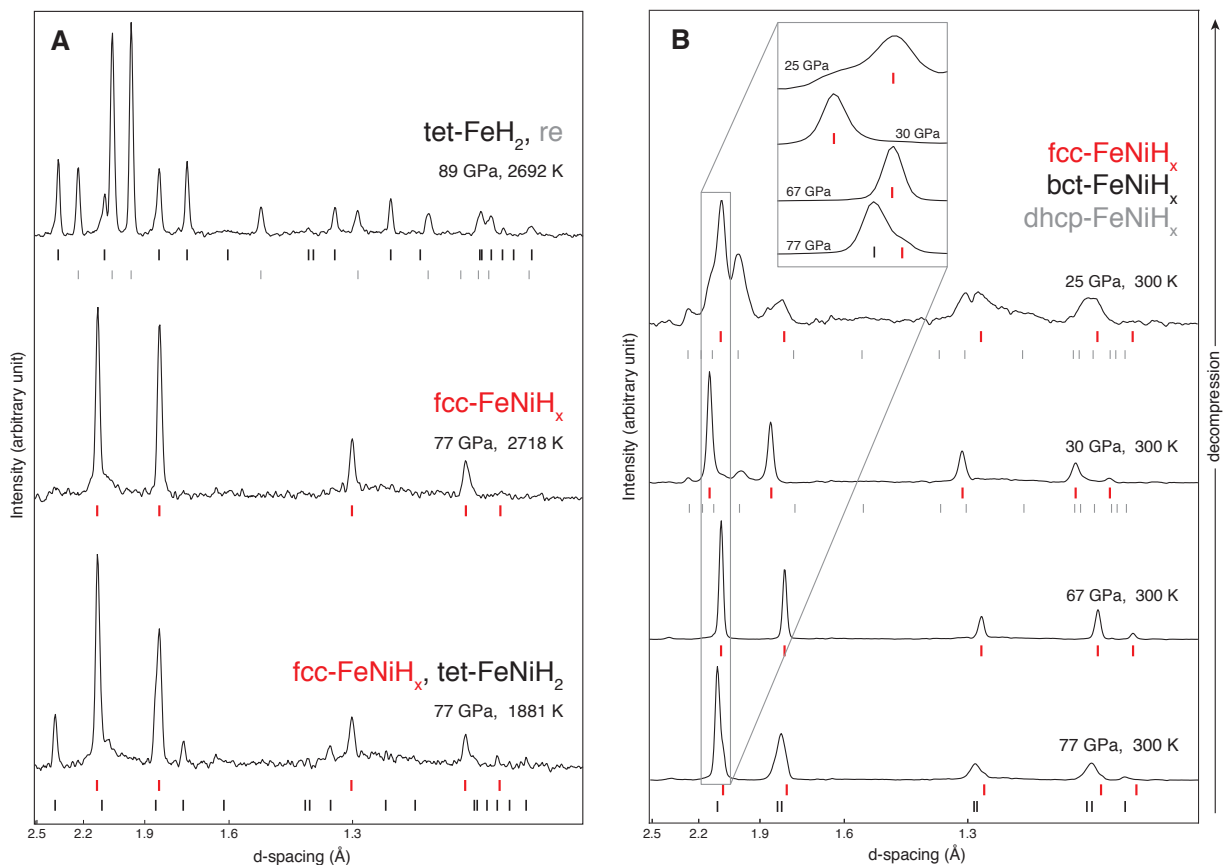


Fig. 1 | X-ray diffraction for fcc-FeH_x and fcc-FeNiH_x. (A) Patterns measured during heating: bottom for the stability of tet-FeNiH₂ and fcc-FeNiH_x (red ticks) at 77 GPa and 1881±150 K; middle for the full conversion from tet-FeNiH₂ (tetragonal, *I4/mmm*, phase) to fcc-FeNiH_x at 77 GPa and 2718±150 K; and top for stability of tet-FeH₂ (black ticks) at 89 GPa and 2692±150 K. (B) Patterns measured at high pressures and 300 K. The *d*-spacings of the fcc-FeNiH_x peak anomalously decreases from 77 GPa to 67 GPa, followed by a “normal” gradual increase in *d*-spacing from 67 to 30 GPa and an abrupt shift to a lower *d*-spacing at 30 GPa. The *d*-spacings of the fcc-FeNiH_x experiences an abrupt shift to a lower *d*-spacing at 25–30 GPa. Below 25 GPa, the peak shifts show expected behavior until the phase converts to bcc-Fe by H loss upon quenching to 1 bar. The inset shows shifts of the 111_{fcc} and 101_{bct} peaks. X-ray diffraction wavelength was 0.3344 Å.

115 by 10.5% and 15.4%, respectively. The pattern of fcc-FeNiH_x at 77 GPa also shows some peak
116 splitting and peak broadening (Fig. 1B), indicating either a distortion of the fcc structure (such
117 as to a body-centered tetragonal structure, bct) or the existence of multiple fcc phases. Our DFT
118 calculations (described further in the text) predict that some fcc-FeH_x (in many cases with an
119 antiferromagnetic (AF) ordering of Fe) could have such a distortion (Table S2).

120 We conducted Rietveld refinements for three models: (i) a single fcc phase, (ii) a mixture of bct
121 + fcc and (iii) a mixture of two fcc phases (the broadening of the 111_{fcc} peak indicates that single bct
122 is unlikely because this peak does not show splitting in bct). Rietveld refinements indicate that the
123 bct + fcc model yields the lowest R_{wp} value at 0.30% (Fig. S1). Such a distortion may result from a
124 large amount of H in the crystal, as indicated by the unusually expanded unit cell. At 77 GPa, the
125 bct phase is dominant with a phase fraction of 92% (Table S3). The second fcc phase also exhibits a
126 unit-cell volume 11% larger than that found in previous reports for FeH_x^{6,10,12}. Even if the peak
127 splitting is ignored and the patterns are forced to fit a single fcc model (Fig. 2), the unit-cell volume
128 remains much greater than previously reported^{6,10,12}.

129 An unusually large unit-cell volume also occurs for thermally quenched fcc-FeH_x at 89 GPa
130 without Ni. However, unlike the Ni-bearing case, we do not observe peak splitting and broadening,
131 and the diffraction patterns are consistent with a single fcc phase. The corresponding fcc phase
132 observed in the Ni-free sample at 89 GPa seems to have a similar unit-cell volume to that of the
133 minor fcc phase observed in the Ni-bearing sample at 77 GPa considering the similar compressibility
134 of these phases (inset in Fig. 2A). We note that our synthesis temperatures for fcc alloys are higher
135 than those of previous reports^{6,7,10,12} by at least 800 K. Considering that H incorporation can
136 increase the unit-cell volume of Fe metal and Ni has little effects on the unit-cell volume of Fe
137 metal (particularly at low Ni content)²⁴, we interpret that both Ni and high temperatures enhance H
138 solubility in Fe metal synthesized in our experiments.

139 The unit-cell volumes of FeNiH_x and FeH_x synthesized at 33 GPa and 77 GPa were measured
140 during decompression (Fig. 2A; data are provided in Table S1). The measured unit-cell volume and
141 compressional behavior of fcc-FeNiH_x between 77 GPa and 67 GPa, is strikingly different from

142 what was reported at the same pressure conditions^{6,10,12}. Upon decompression from the synthesis
143 pressure (77 GPa) down to 70 GPa, we observed a steady *decrease* in the unit-cell volumes, which
144 is the opposite to the expected behavior of crystalline solids under decompression, i.e., volume
145 *increase* (insets in Fig. 1B and 2A). During decompression, the bct distortion also decreases whereas
146 the fraction of fcc phase increases (Table S3). These anomalous compressional behavior can be
147 best explained by the gradual loss of hydrogen for an unusually H-rich FeNi alloy (the bct phase)
148 with decreasing pressure. At 67 GPa, peaks are sharper (Fig. 1B) and almost no peak splittings
149 are observed, consistent with the existence of a single fcc phase. From 67 GPa down to 30 GPa,
150 the unit-cell volume of the fcc phase remains anomalously high, but its decompression behavior
151 appears to be normal. At 30 GPa, the dhcp phase appears in the diffraction patterns. At 25 GPa, the
152 unit-cell volume of the fcc phase drops abruptly. From 25 GPa down to 4 GPa, we observe a gradual
153 decrease in the unit-cell volumes of the fcc and dhcp phases the measured unit-cell volumes of the
154 dhcp and fcc phases agree with those reported for the corresponding phases in the Fe–H system^{6,7}.

155 **Density functional theory calculations for the hydrogen content**

156 How much hydrogen do the unusual volume-expanded fcc phases contain above 30 GPa? Because
157 H escapes from iron metal alloys at 1 bar, quantification of hydrogen content from the recovered
158 samples is not feasible in experiments. In a conventional 4-atom fcc cell, there are 8 tetrahedral and
159 4 octahedral sites where H can be hosted (Fig. 2). Accordingly, H/Fe ratios can range anywhere
160 from 0 up to 3. The incorporation of H into the interstitial sites leads to an expansion of the
161 fcc structure and therefore an increase of its volume with respect to that of H-free fcc-Fe^{6,10,11}.
162 Therefore, previous experimental studies have estimated the H content of synthesized FeH_x phases
163 from the volume difference between fcc-FeH_x and close-packed structured Fe metal, assuming that
164 the volume expansion by H is proportional to the H content. Based on this method, existing reports
165 have estimated H/Fe (or *x*) up to 1.1 for fcc-FeH_x phases synthesized at high pressures^{6,11,12}.

166 However, this method comes with two sources of significant uncertainty on the estimated H
167 content: (i) the volume expansion caused by hydrogen is not directly known for fcc-FeH and

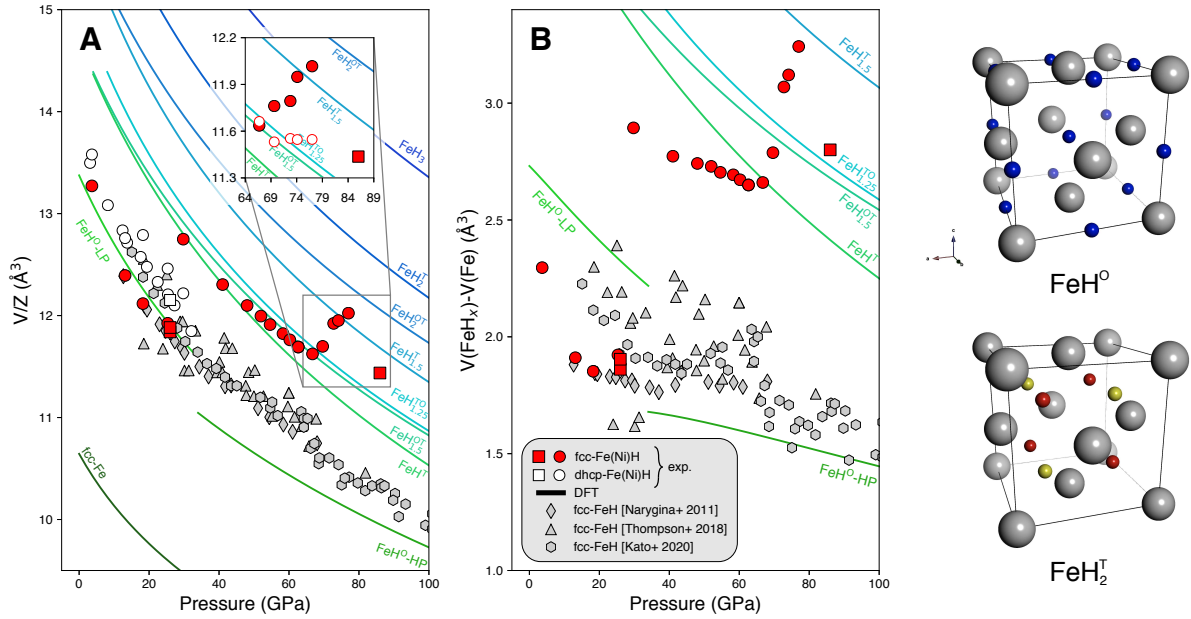


Fig. 2 | Estimate of H contents in the synthesized fcc phases. Squares represent fcc-FeH_x phases and circles represent fcc-FeNiH_x phases. The red and white colors represent fcc and dhcp phases from this study, respectively, and the colored curves are obtained from our DFT calculations. **(A)** Unit-cell volume comparison. The inset shows the unit-cell volumes measured above 70 GPa where peak broadening observed for fcc-FeNiH_x can be explained by the two phase model: bct (solid red) + fcc (open red) (see text for details). **(B)** Unit-cell volume expansion by hydrogen incorporation. We also include data points for FeH_x from previous studies^{6,10,12}. The right panel shows the crystal structures of FeH⁰ and FeH₂^T. The red spheres in FeH₂^T highlight the arrangement of H atoms in a tetrahedral motif which is considered for partial occupancy of H atoms in FeH^T.

168 most studies have used a value of 1.9 \AA^3 per H from fcc-(Fe_{0.65}Mn_{0.29}Ni_{0.09})H_{0.95} at 1 bar²⁵, and
169 (ii) there is no direct measurements of the equation of state (EOS) of fcc-Fe at 300 K because of
170 its instability at 300 K at high pressures. Although the widely used volume expansion value can
171 be supported by the fact that the measured values for other 3d transition metal hydrides in fcc
172 structure are similar²⁶, it is uncertain if it would remain constant at different pressures, temperatures,
173 and compositions, as commonly assumed. Furthermore, it has been generally assumed that H
174 preferentially exists in the octahedral sites. Recently, a neutron diffraction study up to 12 GPa¹¹
175 suggested the possible existence of some H atoms in the tetrahedral sites of fcc-FeH. The study
176 revised the volume expansion to a larger value of 2.22 \AA^3 per H. The new result introduces important
177 additional questions: (i) would the volume expansion be the same for H in the tetrahedral sites and
178 H in the octahedral sites? and (ii) can H enter different interstitial sites in response to changes in
179 pressure and temperature?

180 In an effort to develop a relationship between the volume expansion of a fcc-FeH_x caused by H
181 (and therefore its stoichiometry x) and the content of H, we performed a series of density functional
182 theory (DFT) calculations. For simplification we did not include Ni. This simplification can be
183 supported for the purpose of our DFT calculations in that Ni has little effects on the unit-cell volume
184 of Fe metal phases if the concentration is low²⁴, which is the case for our experiment. In the DFT
185 models, we consider H/Fe ratios between 0 and 3 by using a range of different vacancy configurations
186 (Fig. 2): H in octahedral sites (H^O), in tetrahedral sites (H^T) and with mixed occupancy (H^{OT} or
187 H^{TO} with dominantly occupied octahedral or tetrahedral sites, respectively). We also consider the
188 ferromagnetic (FM) and antiferromagnetic (AM) magnetic ordering of Fe (Table S2).

189 For H/Fe = 1, a model with all H atoms in octahedral sites (FM-FeH^O-LP) has a lower free-
190 energy than with all H in tetrahedral sites (FM-FeH^T), suggesting that H preferentially enters the
191 octahedral sites in a low-H regime. This result supports the view on H substitution in the close-
192 packed structure of iron metal²⁷. The magnetic moment of the FM-FeH^O model decreases with
193 increasing pressure, becoming zero at 34 GPa. Above 34 GPa, however, non-magnetic (NM) FeH^O-
194 HP becomes the lowest energy configuration. The FM-to-NM transition leads to a volume decrease

195 (Fig. 2). For FeH^{T} , we assumed H in four corners of the cubic arrangement in a tetrahedral motif
196 (Fig. 2). Such an arrangement results in cubic symmetry, which is consistent with our experimental
197 results below 70 GPa. In reality, however, FeH^{T} could have some degree of disordering in the
198 tetrahedral vacancies at finite temperatures (i.e., $T > 0$ K), which could affect the energy. For H/Fe
199 $= 1.5$, models with full octahedral occupancy and partial tetrahedral occupancy ($\text{FeH}_{1.5}^{\text{OT}}$) yield lower
200 energies than a model with all H in the tetrahedral sites ($\text{FeH}_{1.5}^{\text{T}}$), consistent again with the notion
201 that H atoms would fill the octahedral sites first.

202 However, $\text{H/Fe} = 2$ models in which all eight tetrahedral sites are occupied (FeH_2^{T}) possess a
203 lower energy than models with fully occupied octahedral sites and partially occupied tetrahedral
204 sites (FeH_2^{OT}). This result suggests that tetrahedral occupancy is important for H-rich systems
205 ($x \geq 2$).

206 In terms of values of the unit-cell volumes, the FM- FeH^{O} -LP model with all H in the octahedral
207 sites agrees well with our fcc- $\text{Fe}(\text{Ni})\text{H}_x$ experimental data below 30 GPa (Fig. 2A). The literature
208 data^{6,10,12} are also in agreement with the unit-cell volume of the FM- FeH^{O} models. Between 30 and
209 70 GPa, our experimental data points systematically lie above the predicted unit-cell volumes of
210 the most stable DFT models for FeH (i.e. FeH^{O}). The DFT models showing agreement with our
211 experimental data above 30–70 GPa are: FM- FeH^{T} , FM- $\text{FeH}_{1.5}^{\text{OT}}$, and FM- $\text{FeH}_{1.25}^{\text{TO}}$. These models all
212 involve tetrahedral occupancy of H and the largest unit-cell volume found for FeNiH_x above 70 GPa
213 is comparable to those of $\text{FeH}_{1.5}^{\text{T}}$ and FeH_2^{OT} . The largest unit-cell volume observed for FeH_x at
214 89 GPa lies between those predicted for $\text{FeH}_{1.25}^{\text{TO}}$ and cubic $\text{FeH}_{1.5}^{\text{OT}}$.

215 Although the good agreement in unit-cell volumes between experimentally observed ones and the
216 DFT models for FeH ($x = 1$) below 30 GPa is encouraging, DFT commonly predicts systematically
217 different unit-cell volumes from experiments. Also, our DFT does not consider disordering for H
218 occupation in interstitial sites, which would result in uncertainties in the comparisons. The thermal
219 expansion effect expected between 0 and 300 K is negligible ($\sim 1\%$) when the configurational H
220 effect dominates (see Text in Supplementary Information, Fig. S2, and Tables S4 and S5).

221 An alternative approach to comparing experiments with DFT simulations is to focus on volume

222 differences (or relative volumes) induced by H instead of absolute volumes. Although similar
223 strategies have been used in previous studies^{6,12} on an empirical basis, the present DFT-based
224 approach exploits the fact that H volume expansion in fcc-Fe models is determined in an internally
225 consistent way. However, an issue for experimental data in this approach is on the choice of a
226 suitable reference system. Because fcc-Fe is not stable at 300 K and high pressure, here we use the
227 well-established EOS of hcp-Fe²⁸ (hcp: hexadonal close packed). We here assume that the volumes
228 of both close-packed structures (fcc and hcp) are sufficiently similar for the comparison, which is
229 reasonable in that the theoretical packing densities of hcp and fcc are the same.

230 Similar to the absolute volume comparison above (Fig. 2A), our data below 30 GPa and the
231 literature data^{6,10,12} fall within the FM-FeH^O models, suggesting $x \approx 1$. At 30–70 GPa, experimental
232 data points are slightly lower than those of the FM-FeH^T model, again supporting the tetrahedral
233 occupancy of H atoms in this pressure range. Finally, the largest volume expansion observed for
234 FeNiH_x at 77 GPa is closer to that of FM-FeH^T_{1.5}, and the volume expansion for FeH_x at 89 GPa is
235 closer to that of FM-FeH^{TO}_{1.25}. The results are, albeit on the lower end, in general agreement with the
236 absolute unit-cell volume comparisons made above. Despite the aforementioned uncertainties, both
237 comparisons support superstoichiometric (i.e. FeH_x with $x > 1$) fcc phases above 70 GPa with the
238 H/Fe ratio between 1.25 and 2 with significant H tetrahedral occupancy. In the 30–70 GPa range,
239 H/Fe can be estimated between 1 and 1.5, again with significant H occupancy of tetrahedral sites.

240 Comparing the experimental setup and composition from previous reports, we interpret that Ni
241 and high-temperature heating in our study promote much higher H/Fe in the close-packed structured
242 fcc phase. In particular, the temperatures achieved in this study are higher than temperatures from
243 previous studies of fcc-FeH_x^{6,10,12} or iron polyhydrides⁷ and are hence more relevant to planetary
244 interiors. Therefore, the large H solubility in densely packed Fe metal alloys observed here has
245 important implications for planets.

246 **Implications**

247 A thick hydrogen-dominant atmosphere would be in contact with silicates and metals at high P – T
248 in the interiors of gas giants in the solar system and exoplanetary systems. In some sub-Neptune
249 planets, such an environment would also exist albeit at lower pressures^{29,30}. The high solubility
250 of H in Fe-Ni dominant core-forming materials we report here, supports the large ingassing and
251 storage of H into the cores of such planets. If a planet has a well differentiated interior with a
252 silicate layer separating the metal of the core from the atmosphere, such metal-hydrogen reaction
253 could be limited. A more likely scenario for an intense H-ingassing can be envisioned during
254 planet formation, in which run-away accretion of H to the core during growth of a large planet
255 would certainly provide sufficient pressures and temperatures for the reaction to occur³¹. Infalling
256 core-forming materials to these types of planets with hydrogen atmospheres will experience high
257 P – T conditions for such reaction³². A giant impact could also shatter a pre-existing core (at least
258 partially) and disperse materials into the warm dense H-rich atmosphere³³. These types of processes
259 would enable hydrogen-metal reaction at high P – T and therefore extensive H-ingassing into the
260 core.

261 According to recent high-pressure experimental studies^{19,20}, a large amount of FeH can form
262 in oxidizing H₂O-rich settings such as the interiors of Neptune-type planets and “waterworld”
263 exoplanets (see reactions 3 and 4 above). Such a process can facilitate significant ingassing of H
264 while oxidizing the silicate layer and limiting the outgassing of H to the atmosphere.

265 We calculated mass-radius relations for H/Fe = 1, 2, 3, and 5 (corresponding to 1.8, 3.5, 5.1, and
266 8.3 wt% H, respectively) considering two structural models of planets: (i) 2-layer planets with a
267 pure metallic core surrounded by a pure H atmosphere, and (ii) single-layer planets where all the H
268 is dissolved into the core (i.e., its composition can be accounted for by a single FeH_{*x*} phase) (Fig. 3).
269 Our experiments support up to H/Fe = 2 in close-packed iron metal with a significant amount of
270 H in tetrahedral sites as well as octahedral sites. If both octahedral and tetrahedral sites are fully
271 filled, up to H/Fe = 3 is possible, which should be investigated by future experiments at higher
272 pressures. For H/Fe > 3, H-H bonding would occur, and our experiments show that Fe-polyhydrides,

273 FeH₂ and FeH₃, can be stabilized at sufficient high temperatures for planetary cores (Fig. 1A).
274 We therefore used FeH₅ polyhydride (the highest H/Fe known so far, assuming that it would be
275 thermally stabilized at higher pressures) reported in⁸ for the calculation.

276 The results show that storing H into the core leads to a large reduction in the radius of a planet
277 (Fig. 3) with respect to a planet where H is completely outgassed to the atmosphere. For example,
278 the radius of a 6M_{Earth} planet with 5.1 wt% hydrogen (H/Fe = 3) would decrease by 35% if all H
279 was stored in the core. This large change in volume is because H can be much more compressed
280 and densely packed under large pressures in the crystal structure of iron metal than when H is a
281 pure phase. Our mass-radius relations are calculated from isothermal EOSs at 0 and 300 K for Fe,
282 FeH_x and H₂. Ignoring thermal effects would not significantly change the mass-radius relations of
283 pure Fe and FeH_x due to their small thermal expansion. However, because the thermal expansion of
284 pure H is much greater, the radius of planets with separate H atmospheres would be much greater
285 than predicted here at higher temperatures, particularly for hot Jupiter-type gas giants. Therefore,
286 the reduction in radius by H storage in the core estimated here is a lower bound.

287 There are currently no experimental data points on the solubility of hydrogen into iron beyond
288 the pressures expected for the Earth and even there the data are limited. While some improvements
289 have been reported³⁴, such a limitation is not different from those associated with many other key
290 phases that have been used in mass-radius plots. However, a DFT study has predicted that Fe
291 would dissolve into H at the conditions relevant to the interior of gas giants like Jupiter (~4 TPa
292 and up to 20,000 K)³⁵ and our experimental observations suggest that hydrogen solubility would
293 continue increasing with pressure and temperature even in dense close-packed metal iron (such as
294 fcc). Lithophile elements are also likely to exist in the interiors of large planets. DFT calculations
295 have predicted a large solubility between lithophile elements (e.g., Mg and Si) and hydrogen^{36,37}.
296 Similar to what we found for FeH_x, the mixed form is denser than pure hydrogen or a H-He mixture,
297 and therefore similar radius effects may apply to those cases. The large H storage in the core of a
298 gas giant can support the “diluted core” model proposed to explain the Juno data³⁸ for Jupiter.

299 For sub-Neptune exoplanets, dissolution of H in the magma ocean at sufficiently high pressure (in

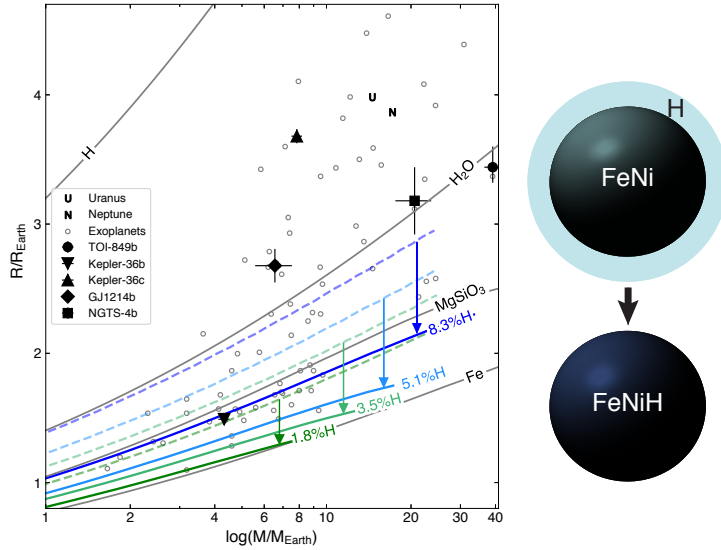


Fig. 3 | Mass-radius relations of hydrogen-storing metal iron cores (the dark colored curves with varying amount of H in wt%). The light colored curves are the mass-radius relations of pure metallic iron with a separate outer envelope of hydrogen for the same amounts of H. The vertical arrows show the radius decrease by storing H in the core for the same bulk compositions (green, teal, light blue, and blue for $\text{H}/\text{Fe} = 1, 2, 3,$ and $5,$ respectively). For comparison, the mass-radius relations for metallic iron (Fe), bridgmanite (MgSiO_3), ice (H_2O), and hydrogen (H) are shown. They are calculated for 300 K. The plot includes the mass and radius of some exoplanets. The gray circles are for exoplanets from NASA exoplanet archive with uncertainties less than 20%.

300 this case approximately 9 GPa) was used to explain the observed sudden decrease in the population
 301 at $R \approx 3R_{\text{Earth}}$, the “radius cliff”³⁰. According to reactions 1, 3, and 4, Fe metal in the early magma
 302 ocean would react with H_2 or H_2O in the atmosphere (or even in the magma ocean) to form FeH_x ,
 303 provided the atmosphere-magma interface reaches sufficient pressures. It is of interest to know if
 304 the “radius cliff” is a representation of conditions where the interface pressure becomes high enough
 305 (because of a thick enough atmosphere) for significant Fe-H alloying to occur.

306 Large exoplanets with unusually high densities such as Kepler-36b, NGTS-4b, and TOI-849b
 307 have been recently discovered and interpreted as the remnant cores of gas giants^{39–41}. Several
 308 hypotheses have been proposed: (i) these planets once had a thicker atmosphere and suffered
 309 massive loss of their atmospheric H, or (ii) they were not able to accrete dense atmospheres either
 310 because of late formation or formation in a region of the protoplanetary disk devoid of gas⁴¹. Our
 311 study suggests the alternative possibility of H storage in the core. For example, the radius of Kepler-

312 36b can be explained by either a 2-layer model Fe-H planet with 1.8 wt% H bulk composition, or a
313 single layer of a H-rich core (8.3% H) (Fig. 3). Although end-member cases, the example reveals
314 that H storage in a core is a plausible explanation of the observation.

315 TOI-849b and NGTS-4b require a thin atmosphere to explain their radii⁴¹. Although efficient
316 packing would make FeH_x much more dense than separate Fe and $x\text{H}$, the density of the H-bearing
317 core would be less than that of a pure Fe core and the mass-radius relation approaches that of
318 MgSiO_3 bridgmanite as the bulk H content of the planet increases (Fig. 3). If the cores of TOI-849b
319 and NGTS-4b contain large amounts of H, the amount of atmospheric H required for explaining
320 their radius would be much smaller and would support the thin atmosphere idea. Could the thin
321 atmospheres then form from H outgassing from the cores? Losing a once thick H atmosphere (likely
322 through hydrodynamic escape), would decrease the pressure originally applied to the core and the
323 solubility of H at shallow core depths would therefore be reduced, resulting in H outgassing of the
324 shallow region. Of course, the compositions of the cores of these planets may be more complicated
325 than pure FeH, and these cores may contain substantial amounts of lithophile elements, which
326 would make them less dense and therefore further reduce the amount of atmospheric H required
327 to explain their observed mass-radius relations. Additionally, H storage would be limited to the
328 maximum H/Fe value of FeH_x being stabilized at high pressures.

329 In conclusion, our high-pressure experiments combined with DFT show that extensive storage
330 of H in the core of large planets is plausible and therefore H storage in the deep interior should be
331 considered in modeling planet formation and characterizing giant planets.

332 **Acknowledgments**

333 **Funding:** The work has been supported by the NASA (80NSSC18K0353) and NSF (EAR1921298
334 and AST2005567). H.P., P.B., and S.-H.S. were supported partially by the Keck Foundation (PI:
335 P. Buseck). The results reported herein benefit from collaborations and information exchange
336 within NASA's Nexus for Exoplanet System Science (NExSS) research coordination network
337 sponsored by NASA's Science Mission Directorate. A.V.G.C. gratefully acknowledges ASU's

338 supercomputing resources. B.C. acknowledges the support from NSF (EAR-1555388, EAR-
339 1829273). The synchrotron experiments were conducted at GeoSoilEnviroCARS (University of
340 Chicago, Sector 13), Advanced Photon Source (APS). GeoSoilEnviroCARS is supported by the NSF-
341 Earth Science (EAR-1634415) and DOE-GeoScience (DE-FG02-94ER14466). APS is supported by
342 DOE-BES under contract DE-AC02-06CH11357. **Author contributions:** H.P. designed the study,
343 performed the experiments, analyzed and interpreted the results and wrote the paper. A.V.G.C.
344 performed the DFT calculations and wrote the paper. B.C. provided samples and edited the paper.
345 S.C., E.G., and V.B.P. provided synchrotron XRD support and edited the paper. P.R.B. provided
346 funding and edited the paper. S.-H.S. designed and supervised the study, interpreted the results,
347 provided fundings and wrote the paper. **Competing interests:** The authors declare no conflict of
348 interest. **Data and materials availability:** The experimental data for this paper are available by
349 contacting SHDShim@asu.edu.

350 References

- 351 1. Birch, F. Density and composition of mantle and core. *Journal of geophysical research* **69**,
352 4377–4388 (1964).
- 353 2. Poirier, J.-P. Light elements in the earth's outer core: a critical review. *Physics of the earth and*
354 *planetary interiors* **85**, 319–337 (1994).
- 355 3. Deemyad, S. *et al.* Pulsed laser heating and temperature determination in a diamond anvil cell.
356 *Review of scientific instruments* **76**, 125104 (2005).
- 357 4. Goncharov, A. F. *et al.* X-ray diffraction in the pulsed laser heated diamond anvil cell. *Review*
358 *of Scientific Instruments* **81**, 113902 (2010).
- 359 5. Seager, S. & Deming, D. Exoplanet atmospheres. *Annual Review of Astronomy and Astrophysics*
360 **48**, 631–672 (2010).

- 361 6. Narygina, O. *et al.* X-ray diffraction and mössbauer spectroscopy study of fcc iron hydride feh
362 at high pressures and implications for the composition of the earth's core. *Earth and Planetary*
363 *Science Letters* **307**, 409–414 (2011).
- 364 7. Pépin, C. M., Dewaele, A., Geneste, G., Loubeyre, P. & Mezouar, M. New iron hydrides under
365 high pressure. *Physical review letters* **113**, 265504 (2014).
- 366 8. Pépin, C., Geneste, G., Dewaele, A., Mezouar, M. & Loubeyre, P. Synthesis of feh5: A layered
367 structure with atomic hydrogen slabs. *Science* **357**, 382–385 (2017).
- 368 9. Iizuka-Oku, R. *et al.* Hydrogenation of iron in the early stage of earth's evolution. *Nature*
369 *communications* **8**, 1–7 (2017).
- 370 10. Thompson, E. *et al.* High-pressure geophysical properties of fcc phase fehx. *Geochemistry,*
371 *Geophysics, Geosystems* **19**, 305–314 (2018).
- 372 11. Ikuta, D. *et al.* Interstitial hydrogen atoms in face-centered cubic iron in the earth's core.
373 *Scientific reports* **9**, 1–8 (2019).
- 374 12. Kato, C. *et al.* Stability of fcc phase feh to 137 gpa. *American Mineralogist* **105**, 917–921
375 (2020).
- 376 13. Drozdov, A., Eremets, M., Troyan, I., Ksenofontov, V. & Shylin, S. I. Conventional super-
377 conductivity at 203 kelvin at high pressures in the sulfur hydride system. *Nature* **525**, 73–76
378 (2015).
- 379 14. Drozdov, A. *et al.* Superconductivity at 250 k in lanthanum hydride under high pressures.
380 *Nature* **569**, 528–531 (2019).
- 381 15. Bolton, S. J. *et al.* Jupiter's interior and deep atmosphere: The initial pole-to-pole passes with
382 the juno spacecraft. *Science* **356**, 821–825 (2017).

- 383 16. Sagatova, D., Gavryushkin, P., Sagatov, N., Medrish, I. & Litasov, K. Phase diagrams of
384 iron hydrides at pressures of 100–400 gpa and temperatures of 0–5000 k. *JETP Letters* **111**,
385 145–150 (2020).
- 386 17. Badding, J. V., Hemley, R. & Mao, H. High-pressure chemistry of hydrogen in metals: In situ
387 study of iron hydride. *Science* **253**, 421–424 (1991).
- 388 18. Elkins-Tanton, L. T. & Seager, S. Coreless terrestrial exoplanets. *The Astrophysical Journal*
389 **688**, 628 (2008).
- 390 19. Ohtani, E., Hirao, N., Kondo, T., Ito, M. & Kikegawa, T. Iron-water reaction at high pressure
391 and temperature, and hydrogen transport into the core. *Physics and chemistry of minerals* **32**,
392 77–82 (2005).
- 393 20. Yuan, L. *et al.* Chemical reactions between fe and h₂o up to megabar pressures and implications
394 for water storage in the earth’s mantle and core. *Geophysical Research Letters* **45**, 1330–1338
395 (2018).
- 396 21. McDonough, W. 3.16–compositional model for the earth’s core. *Treatise on geochemistry*
397 547–568 (2003).
- 398 22. Zhang, L. & Fei, Y. Effect of ni on fe–fes phase relations at high pressure and high temperature.
399 *Earth and Planetary Science Letters* **268**, 212–218 (2008).
- 400 23. Shibazaki, Y. *et al.* High-pressure and high-temperature phase diagram for fe_{0.9}ni_{0.1}-h alloy.
401 *Physics of the Earth and Planetary Interiors* **228**, 192–201 (2014).
- 402 24. Mao, H., Wu, Y., Chen, L., Shu, J. & Jephcoat, A. P. Static compression of iron to 300 gpa and
403 fe_{0.8}ni_{0.2} alloy to 260 gpa: Implications for composition of the core. *Journal of Geophysical*
404 *Research: Solid Earth* **95**, 21737–21742 (1990).
- 405 25. Antonov, V., Belash, I., Ponomarev, B., Ponyatovskii, E. & Thiessen, V. Magnetic properties of
406 hydrogen solid solutions in fe–ni–mn alloys. *physica status solidi (a)* **52**, 703–710 (1979).

- 407 26. Fukai, Y. *The metal-hydrogen system: basic bulk properties*, vol. 21 (Springer Science &
408 Business Media, 2006).
- 409 27. Antonov, V. Phase transformations, crystal and magnetic structures of high-pressure hydrides
410 of d-metals. *Journal of alloys and compounds* **330**, 110–116 (2002).
- 411 28. Dewaele, A. *et al.* Quasihydrostatic equation of state of iron above 2 mbar. *Physical Review*
412 *Letters* **97**, 215504 (2006).
- 413 29. Rogers, L. A. Glimpsing the compositions of sub-neptune-size exoplanets. *Proceedings of the*
414 *International Astronomical Union* **8**, 247–251 (2013).
- 415 30. Kite, E. S., Fegley Jr, B., Schaefer, L. & Ford, E. B. Superabundance of exoplanet sub-neptunes
416 explained by fugacity crisis. *The Astrophysical Journal Letters* **887**, L33 (2019).
- 417 31. Boley, A. C. The two modes of gas giant planet formation. *The Astrophysical Journal Letters*
418 **695**, L53 (2009).
- 419 32. Valletta, C. & Helled, R. The deposition of heavy elements in giant protoplanetary atmospheres:
420 The importance of planetesimal–envelope interactions. *The Astrophysical Journal* **871**, 127
421 (2019).
- 422 33. Liu, S.-F. *et al.* The formation of Jupiter’s diluted core by a giant impact. *Nature* **572**, 355–357
423 (2019).
- 424 34. Smith, R. F. *et al.* Equation of state of iron under core conditions of large rocky exoplanets.
425 *Nature Astronomy* **2**, 452–458 (2018).
- 426 35. Wahl, S. M., Wilson, H. F. & Militzer, B. Solubility of iron in metallic hydrogen and stability
427 of dense cores in giant planets. *The Astrophysical Journal* **773**, 95 (2013).
- 428 36. Wilson, H. F. & Militzer, B. Rocky core solubility in Jupiter and giant exoplanets. *Physical*
429 *Review Letters* **108**, 111101 (2012).

- 430 37. González-Cataldo, F., Wilson, H. F. & Militzer, B. Ab initio free energy calculations of the
431 solubility of silica in metallic hydrogen and application to giant planet cores. *The Astrophysical*
432 *Journal* **787**, 79 (2014).
- 433 38. Wahl, S. M. *et al.* Comparing Jupiter interior structure models to Juno gravity measurements
434 and the role of a dilute core. *Geophysical Research Letters* **44**, 4649–4659 (2017).
- 435 39. Carter, J. A. *et al.* Kepler-36: A pair of planets with neighboring orbits and dissimilar densities.
436 *Science* **337**, 556–559 (2012).
- 437 40. West, R. G. *et al.* NGTS-4b: A sub-neptune transiting in the desert. *Monthly Notices of the*
438 *Royal Astronomical Society* **486**, 5094–5103 (2019).
- 439 41. Armstrong, D. J. *et al.* A remnant planetary core in the hot-Neptune desert. *Nature* **583**, 39–42
440 (2020).

441 **Materials and methods**

442 **High-pressure and high-temperature synchrotron X-ray diffraction**

443 Two different starting materials were used: pure metallic iron (reagent grade powder from Alfa
444 Aesar), and metallic Fe-6.5(4)%Ni. The Fe-6.5(4)%Ni alloy was synthesized by quenching the
445 Fe-Ni liquid at 1973 K and 1 bar. The starting material of Fe-Ni mixture was contained in an
446 Al₂O₃ ceramic crucible, which was first evacuated in a fused quartz tube by a high-vacuum system
447 (turbo-molecular pump) prior to the introduction of a pressurized atmosphere of argon. The Fe-Ni
448 mixture was then heated until fully molten up to 1973 K by a 50–200 kHz, 15 kW of induction
449 heating unit¹. We compressed the sample in the diamond anvil cell, with diamond culet sizes
450 ranging between 200 and 150 μm to achieve pressures between 26 and 89 GPa. We drilled the
451 sample chamber in a pre-compressed rhenium gasket, which we later coated with gold (≥ 80 Å in
452 thickness) to prevent embrittlement by hydrogen during experiments². We loaded the sample as
453 a foil into the sample chamber, which was propped on both sides by pieces of the same material
454 to avoid full contact with the anvils and provide better laser coupling during heating. We loaded
455 a piece of ruby and a piece of gold for pressure measurement. These grains were loaded apart
456 from the sample to avoid contamination during laser heating. Pressure was measured before and
457 after laser-heating. Pure hydrogen gas was then loaded into the sample chamber using a loading
458 system at Arizona State University. We acquired X-ray diffraction (XRD) patterns at *in situ* high
459 pressure and high temperature in the laser-heated diamond-anvil cell at the 13-IDD beamline of the
460 GSECARS sector of the Advanced Photon Source. A $3 \times 4 \mu\text{m}^2$ monochromatic X-ray beam with
461 energy of 30 keV or 37 keV was co-axially aligned with double-sided near-infrared laser-heating
462 beam providing a $15 \times 20 \mu\text{m}^2$ heating spot. We first compressed the sample to the target pressure at
463 300 K. Pressure is measured using the equation of state of gold³. Laser-heating with pure hydrogen
464 is challenging because high temperatures enhance its already high reactivity and high diffusion
465 at high pressure making the diamond anvil and gaskets brittle, increasing the likelihood for anvil
466 failure. However, we mitigate these problems using the gold coating of gaskets² and a pulsed-laser

467 heating⁴ providing short heating durations 1 μ s pulses). The laser pulse is synchronized with gated
468 X-ray and temperature detectors to allow XRD acquisition at in situ high P - T ⁵. To obtain XRD
469 patterns in sufficiently high quality, we generate a series of 10^5 pulses to a repetition rate of 10 kHz
470 and accumulate the obtained diffraction patterns during heating. The temperature is calculated
471 by fitting a Planck equation to the thermal radiation spectra collected on both sides of the DAC
472 assuming a grey-body approximation. We collected 2D diffraction images using a Pilatus 1M
473 CdTe detector. We used a LaB₆ standard to calibrate and correct distortions and detector distance
474 (\sim 200 mm) during integration from 2D images to 1D patterns in the Dioptas software⁶. We used
475 the PeakPo software package⁷ for peak identification and unit-cell fitting. Rietveld refinements
476 were performed on selected diffraction patterns for fcc-FeH in the general structure analysis system
477 (GSAS-II)⁸.

478 **Density Functional Theory (DFT) calculations**

479 All spin-density functional calculations on the FeH_{*x*} ($x = 0\sim 3$) systems were carried out using
480 the VASP code⁹ and both the Perdew-Burke-Ernzerhof (PBE) version of generalized gradient
481 approximation (GGA) for exchange and correlation¹⁰ and the Ceperley-Alder (CA) version of
482 local-density approximation (LDA)¹¹. Core state were treated using the projector augmented
483 wave (PAW)¹² method in which H [$1s^1$] and Fe [$2p^63d^74s^1$] electrons were explicitly treated.
484 Convergence was carefully tested for each system, and overall we found that a plane-wave basis
485 with an energy cutoff of 500 eV in combination with $16\times 16\times 16$ Monkhorst-Pack k -point grids led
486 to energy, force and stress convergence of 0.1 meV, 10^{-5} eV/Å and 0.1 kBar, respectively. Thorough
487 structure optimizations were first performed on all systems in the static lattice approximation (no
488 zero-point energy or thermal corrections). Accurate compression equations of state (EOS) for each
489 system were obtained using the isochoric approach, in which the static-lattice energy is evaluated
490 over a range of volumes (typically 20) surrounding the static-lattice minimum, including several
491 expanded structures. At each volume the shape and internal atomic positions are fully optimized,
492 yielding an energy-volume data set which was then fit to 2nd order Birch-Murnaghan (BM) form^{13,14}

493 to obtain the static-lattice ground state energy, volume, bulk modulus and bulk modulus derivative
494 at $P = 0$. The magnetization of the system was also carefully analyzed at each volume to establish
495 magnetic state, and identify magnetic phase changes.

496 In fcc-FeH_x, H is hosted in the octahedral and tetrahedral sites. Different site occupancies for
497 hydrogen were therefore investigated (Table S2). We also investigated different magnetic states
498 (ferromagnetic (FM) and antiferromagnetic (AM)) and extracted the corresponding magnetic
499 moment (μ) for each magnetic phase. While a range of possibility exists for antiferromagnetic
500 ordering, for the sake of simplicity, we consider alternating spin directions along the c axis of the
501 fcc lattice. Such a setup breaks the cubic symmetry of fcc resulting in a deviation of the c axis and a
502 bct structure. We also found the bct structure to be stable for some FM models, likely because of
503 the tetrahedral occupancy for H atoms in these models. For a same composition, different hydrogen
504 occupancies in octahedral and/or tetrahedral sites yield different minimum energies. Because the
505 fitting for experimental data indicates that the c/a ratio should not exceed 1.013 (Table SS3), we
506 therefore do not consider the calculated bct structures, for which $c/a \geq 1.03$. We calculated the
507 compression of these phases at 0 K and up to 190 GPa.

508 **Mass-radius calculations**

509 The mass-radius relations were calculated by the Burnman code¹⁵ with some optimization for
510 improved convergence. We calculated mass-radius relations of FeH_x for $x = 1, 2, 3,$ and 5
511 (corresponding to 1.8, 3.5, 5.1, and 8.3 wt% H, respectively), which can be viewed as hypothetical
512 single phase (i.e., one layer) planets (the colored solid curves in Fig. 3). Mass-radius relations were
513 also calculated for hypothetical two layer planets with the same bulk compositions but where the
514 core is pure metallic Fe and is surrounded by a pure hydrogen envelope (the colored dashed curves
515 in Fig. 3). The mass-radius relations were calculated without considering thermal effects. Indeed,
516 temperatures are highly variable in exoplanets and, more importantly, temperature effects are lesser
517 than pressure effects¹⁶.

518 We used the EOSs of FeH_x in fcc configuration obtained from our DFT calculations (Table S2).

519 We used EOS of the following models: FM FeH^O, FM FeH₂^{OT} and FM FeH₃. For FeH, we use the
520 high pressure configuration with zero net magnetic moment which was the most stable form. In the
521 case of FeH₅, hydrogen atoms form inter-hydrogen bonding¹⁷, unlike the case of fcc-FeH_x with
522 $x \leq 3$. For FeH₅, we use the EOS from Pépin et al.¹⁷. The EOSs of pure metallic iron and MgSiO₃
523 bridgmanite were obtained from the SLB2011 parameter set by Stixrude et al.¹⁸. The EOSs of H₂O
524 ice and hydrogen we use are from Seager et al.¹⁶ and Loubeyre et al.¹⁹, respectively.

525 **References**

- 526 1. Nasch, P. M., Manghnani, M. & Secco, R. A modified ultrasonic interferometer for sound
527 velocity measurements in molten metals and alloys. *Review of scientific instruments* **65**,
528 682–688 (1994).
- 529 2. Pépin, C. M., Dewaele, A., Geneste, G., Loubeyre, P. & Mezouar, M. New iron hydrides under
530 high pressure. *Physical review letters* **113**, 265504 (2014).
- 531 3. Ye, Y., Prakapenka, V., Meng, Y. & Shim, S.-H. Intercomparison of the gold, platinum, and
532 mgo pressure scales up to 140 gpa and 2500 k. *Journal of Geophysical Research: Solid Earth*
533 **122**, 3450–3464 (2017).
- 534 4. Deemyad, S. *et al.* Pulsed laser heating and temperature determination in a diamond anvil cell.
535 *Review of scientific instruments* **76**, 125104 (2005).
- 536 5. Goncharov, A. F. *et al.* X-ray diffraction in the pulsed laser heated diamond anvil cell. *Review*
537 *of Scientific Instruments* **81**, 113902 (2010).
- 538 6. Prescher, C. & Prakapenka, V. B. Dioptas: a program for reduction of two-dimensional x-ray
539 diffraction data and data exploration. *High Pressure Research* **35**, 223–230 (2015).
- 540 7. Shim, S.-H. PeakPo - A python software for X-ray diffraction analysis at high pressure and
541 high temperature (2017). URL <https://doi.org/10.5281/zenodo.810200>.

- 542 8. Toby, B. H. & Von Dreele, R. B. Gsas-ii: the genesis of a modern open-source all purpose
543 crystallography software package. *Journal of Applied Crystallography* **46**, 544–549 (2013).
- 544 9. Kresse, G. & Furthmüller, J. Efficient iterative schemes for ab initio total-energy calculations
545 using a plane-wave basis set. *Physical review B* **54**, 11169 (1996).
- 546 10. Perdew, J. P., Burke, K. & Ernzerhof, M. Generalized gradient approximation made simple.
547 *Physical review letters* **77**, 3865 (1996).
- 548 11. Ceperley, D. M. & Alder, B. J. Ground state of the electron gas by a stochastic method. *Physical*
549 *Review Letters* **45**, 566 (1980).
- 550 12. Kresse, G. & Joubert, D. From ultrasoft pseudopotentials to the projector augmented-wave
551 method. *Physical review b* **59**, 1758 (1999).
- 552 13. Birch, F. Finite elastic strain of cubic crystals. *Physical review* **71**, 809 (1947).
- 553 14. Murnaghan, F. The compressibility of media under extreme pressures. *Proceedings of the*
554 *national academy of sciences of the United States of America* **30**, 244 (1944).
- 555 15. Cottar, S., Heister, T., Rose, I. & Unterborn, C. Burnman: A lower mantle mineral physics
556 toolkit. *Geochemistry, Geophysics, Geosystems* **15**, 1164–1179 (2014).
- 557 16. Seager, S., Kuchner, M., Hier-Majumder, C. & Militzer, B. Mass-radius relationships for solid
558 exoplanets. *The Astrophysical Journal* **669**, 1279 (2007).
- 559 17. Pépin, C., Geneste, G., Dewaele, A., Mezouar, M. & Loubeyre, P. Synthesis of feh5: A layered
560 structure with atomic hydrogen slabs. *Science* **357**, 382–385 (2017).
- 561 18. Stixrude, L. & Lithgow-Bertelloni, C. Thermodynamics of mantle minerals-ii. phase equilibria.
562 *Geophysical Journal International* **184**, 1180–1213 (2011).
- 563 19. Loubeyre, P. *et al.* X-ray diffraction and equation of state of hydrogen at megabar pressures.
564 *Nature* **383**, 702–704 (1996).

SM1 **Supplementary Information**

SM2 **Thermal effects in DFT calculations**

SM3 Our primary motivation for adopting generalized gradient approximation (GGA) in our Fe-H system
SM4 simulations is that the local density approximation (LDA) treatment of the reference elemental iron
SM5 is well-known to predict the incorrect ground-state structure (fcc instead of bcc) and a corresponding
SM6 vanishing magnetization¹. Here we show that although systematic application of quasi-harmonic
SM7 thermodynamic corrections (based on phonons) leads to the correct qualitative description of
SM8 iron's ground state in the LDA, only the GGA gives predictions consistent with observed values.
SM9 Accordingly we applied the same *ab initio* thermodynamics scheme to fcc-based FeH phases.

SM10 Finite temperature thermodynamic corrections to the static-lattice equation of state (EOS) in
SM11 Fe-H systems were obtained using phonon spectra generated by the Phonopy code² in conjunction
SM12 with the density functional perturbation theory feature available in Vienna Ab initio Simulation
SM13 Package (VASP). Static-lattice enthalpies were first obtained by direct optimization of volume at a
SM14 series of fixed pressures. As an internal consistency check we verified that the pressure extracted
SM15 from a Birch-Murnaghan (BM) fit to the resulting energy-volume data for each phase yielded values
SM16 which differed from the input pressures by <0.2 GPa. Using the phonons calculated at the latter
SM17 volumes by Phonopy we obtain a quasiharmonic approximation to the “constrained” Helmholtz
SM18 energy as a function of temperature³. After testing a wide range of analytic representation we found
SM19 that the simple functional form $F_{th}(V|T) = A(T) + B(T)V + C(T)/V$ is remarkably accurate over wide
SM20 range of strains and temperatures. The thermal EOS corresponding to the Gibbs Energy minimum
SM21 volume at finite T and P was then obtained by combining the static-lattice enthalpies with $F_{th}(V|T)$
SM22 and repeating the BM fitting as function of temperature. Beside the compression EOS at finite
SM23 temperatures, this procedure also yields the coefficient of thermal expansion (CTE), temperature
SM24 dependence of the bulk modulus and its derivative, and general thermodynamic quantities obtainable
SM25 from derivatives of the free energy. The principal outcomes for elemental Fe are shown in Table SS4
SM26 which shows that the thermally corrected LDA values yield a semi-qualitative description of

SM27 observed behavior, while the corresponding GGA values show excellent agreement with experiment
SM28 and previous *ab initio* estimates⁴.

SM29 We next applied the same thermodynamic correction prescription to the systems FM-FeH^T
SM30 and FM-FeH^O-LP. In the latter two systems all phonon frequencies throughout the Brillouin zone
SM31 were found to be real indicating dynamic stability. However, a number of imaginary branches
SM32 were found in the NM-FeH^O-HP system precluding the calculation of thermal corrections. This
SM33 suggests that the NM-FeH^O-HP phase is would not be quenchable to ambient pressure, consistent
SM34 with experimental observations. Table SS5 compares the static and 300 K-corrected EOS for bcc-Fe,
SM35 FM-FeH^T, and FM-FeH^O-LP. The important conclusion from these simulations in the context of
SM36 the present study is that the inclusion of 300 K corrections essentially shift the reference bcc-Fe
SM37 and FM-FeH^O-LP system volumes upward by $\sim 2\%$ while softening the bulk moduli by $\sim 5\text{--}10\%$.
SM38 However, in the case of the FM-FeH^T we find a surprising and apparently anomalous behavior
SM39 associated with a stiffening of the lattice upon heating ($\Delta B \simeq 14\%$), and a corresponding negative
SM40 thermal expansion (NTE) of approximately -2.7%). This phenomenon can be traced to anomalous
SM41 nearly-volume-independent branches associated with transverse acoustic modes involving protons.
SM42 Similar behavior has recently been predicted in magnesium-nickel hydrides⁵. These trends are
SM43 depicted graphically in Fig. SS2, which demonstrate that largest effect of the *ab initio* thermal
SM44 corrections occurs near ambient pressure with volume corrections of $\sim 2\%$, and much smaller
SM45 deviations at higher pressures.

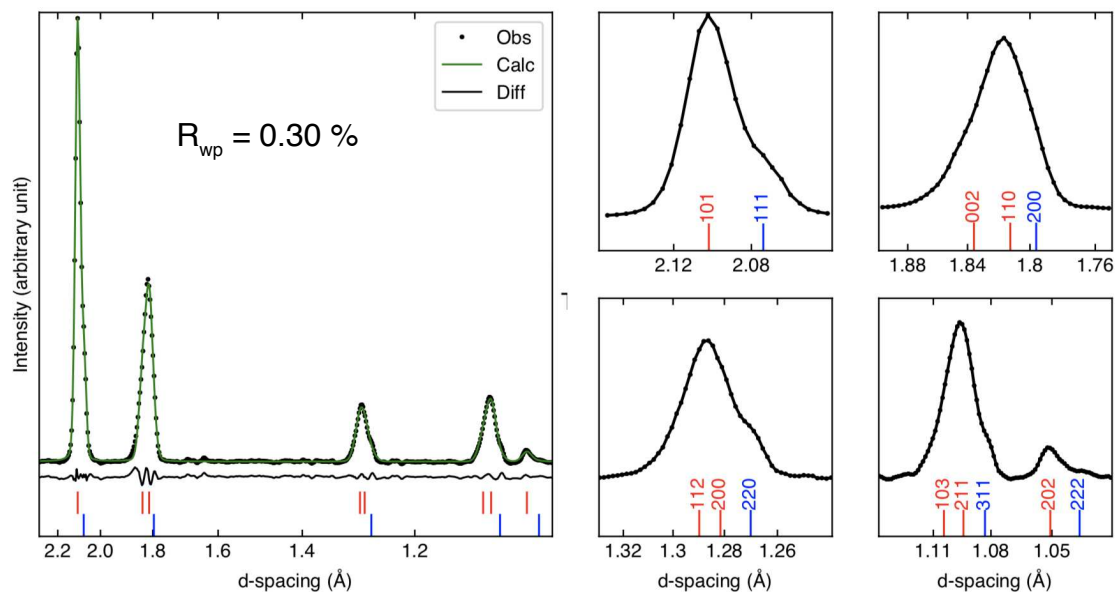


Fig. S1 | Rietveld refinement for fcc-FeNiH_x at 77 GPa after temperature quench from 2718 K. The fit was performed for a bct + fcc mixture with calculated unit-cell volumes of 24.034 Å³/Z and 46.188 Å³/Z, respectively, yield a residual $R_{wp} = 0.30\%$. Calculated peak positions for each phase are shown by red (bct) and blue (fcc) ticks, respectively. We also show magnified angle ranges emphasizing peak splitting caused by the presence of the two phases. X-ray diffraction wavelength was 0.3344 Å.

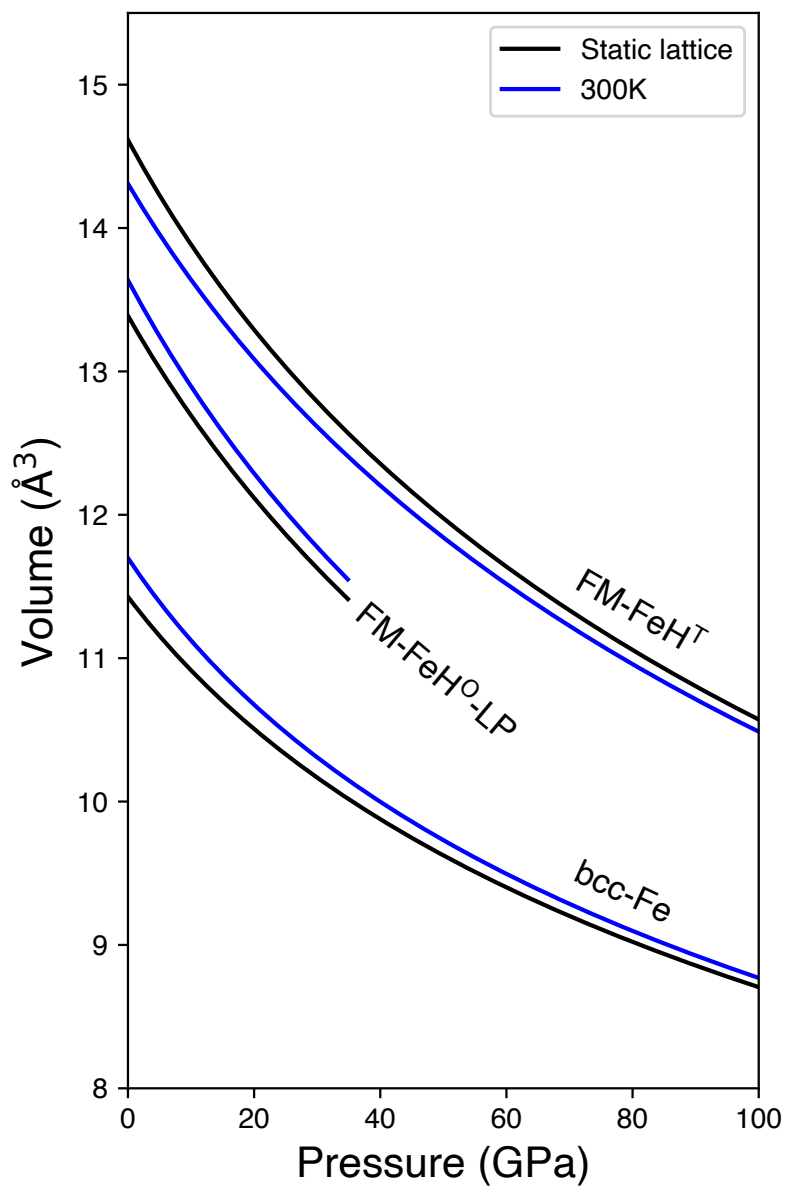


Fig. S2 | Effect of thermal corrections from 0 to 300 K on the static equations of state of bcc-Fe, FM-FeH^T and FM-FeH^O-LP from DFT calculations.

Tab. S1 | Pressure and volume data measured for Fe(Ni)H_x phases at 300 K during decompression. Synthesis pressure–temperature conditions are given in the first column. For Fe-Ni-H synthesized at 77 GPa and 2720 K, we present two different fitting results (fcc and fcc + bct) for unit-cell volumes at 70–77 GPa where we found peak splittings and broadenings. Uncertainties on the last digit(s) are shown in parenthesis.

Run	Pressure (GPa)	Volume (Å ³)			
		dhcp	fcc	fcc + bct	
FeNiH _x	3(1)	53.99(2)			
32 GPa	8(1)	52.33(16)			
2500–2790 K	12(1)	51.34(5)			
	14(1)	50.86(3)			
	18(1)	50.3(7)			
	19(1)	49.91(6)			
	22(2)	49.32(3)			
	25(2)	48.83(3)			
	27(2)	48.4(5)			
	32(2)	47.39(5)			
	FeNiH _x	4(1)	54.00(75)	53.09(73)	
77 GPa	13(1)	49.59(32)	49.57(19)		
1880–2720 K	18(1)	50.24(66)	48.47(20)		
	25(2)	50.08(81)	47.70(38)		
	30(2)	49.38(25)	51.00(4)		
	41(3)		49.22(1)		
	48(3)		48.39(2)		
	52(4)		47.98(3)		
	55(4)		47.65(1)		
	58(4)		47.29(1)		
	60(4)		47.05(2)		
	63(4)		46.77(1)		
	67(5)		46.50(1)		
	70(5)		46.79(6)	46.13(1)	47.05(8)
	73(5)		47.69(4)	46.21(9)	47.17(5)
74(5)		47.80(12)	46.19(7)	47.79(3)	
77(5)		48.10(34)	46.19(12)	48.07(4)	
FeH _x	26(2)	47.29(14)	47.36(9)		
26 GPa					
1170–2180 K					
FeH _x	26(2)	48.61(14)	47.53(9)		
26 GPa					
2600 K					
FeH _x	89(6)		45.75(1)		
89 GPa					
1611–2823 K					

Tab. S2 | Density-functional theory (DFT) results for Fe-H phases in fcc structures at 1 bar and 0 K. Some configurations resulted in bct type distortions ($c/a \neq 1$). For bct, we include models with $c/a \leq 1.1$, based on our experimental observations. E_0 : energy; V_0 : unit-cell volume per Fe; K_0 : bulk modulus; K'_0 : pressure derivative of bulk modulus; μ : magnetic moment; Comp: composition; FM: ferromagnetic; AF: anti-ferromagnetic; LP: pressures below 34 GPa; HP: pressures above 34 GPa; H^O : H occupancy in the octahedral sites (4 sites per 4Fe); H^T : H occupancy in the tetrahedral sites (8 sites per 4Fe); a : H^T in super-tetrahedral motif, $(1/4, 1/4, 1/4)$, $(3/4, 3/4, 1/4)$, $(1/4, 3/4, 3/4)$, and $(3/4, 1/4, 3/4)$; b : H^O at the body center; c : H^T at $(1/4, 1/4, 1/4)$ and $(1/4, 3/4, 1/4)$; d : H^T at $(1/4, 1/4, 1/4)$ and $(3/4, 3/4, 3/4)$; e : H^T at $(1/4, 1/4, 1/4)$, $(1/4, 3/4, 1/4)$, $(3/4, 1/4, 1/4)$, $(3/4, 3/4, 1/4)$, $(1/4, 1/4, 3/4)$, and $(3/4, 3/4, 3/4)$.

Comp	Model	H^O	H^T	c/a	E_0 (eV/Z)	V_0 ($\text{\AA}^3/Z$)	K_0 (GPa)	K'_0	μ_B
Fe (fcc)	FM				-8.30885	10.644	172.4	6.91	1.02
FeH	FM-T	0/4	$4/8^a$		-11.70512	14.697	169.2	3.57	2.16
	FM-O-LP	4/4	0/8		-11.81695	13.375	173.5	4.40	2.10
	NM-O-HP	4/4	0/8		-11.65965	12.181	286.2	4.02	0.00
	AF-O	4/4	0/8		-11.67440	12.298	259.1	4.31	0.00
FeH _{1.25}	FM-TO	$1/4^b$	$4/8^a$		-12.38468	15.105	148.3	4.54	2.12
FeH _{1.5}	FM-OT-A	4/4	$2/8^c$	1.03	-13.22253	14.819	167.3	4.22	1.87
	FM-OT-B	4/4	$2/8^d$		-13.30977	15.881	144.5	4.48	2.06
	FM-T	0/4	$6/8^e$		-13.01773	14.708	174.4	4.24	1.87
FeH ₂	FM-T	0/4	8/8		-14.94413	16.807	160.9	4.23	1.77
	AF-T	0/4	8/8	1.03	-14.70432	16.460	157.6	4.71	0.00
	FM-OT	4/4	$4/8^a$		-14.32160	15.890	175.3	4.32	1.63
FeH ₃	FM	4/4	8/8		-16.67097	18.043	179.3	4.26	0.79

Tab. S3 | Rietveld analysis results for the diffraction patterns above 66 GPa. V is the unit-cell volume; c/a is the axial ratio of bct converted to a pseudo fcc cell ($(c/a)_{\text{fcc}} = (c/a)_{\text{bct}} / \sqrt{2}$); f is the phase fraction; R_{wp} is the fit residual.

P (GPa)	bct + fcc						fcc + fcc					fcc		
	bct			fcc			fcc		fcc			R_{wp}	V (\AA^3)	R_{wp}
	V (\AA^3)	c/a	f	V (\AA^3)	f	R_{wp}	V (\AA^3)	f	V (\AA^3)	f				
77(5)	48.068(42)	1.0129(4)	0.916(1)	46.188(122)	0.084	0.295	48.156(63)	0.918(20)	46.419(131)	0.082	0.705	48.070(17)	0.972	
74(5)	47.794(30)	1.0121(3)	0.823(18)	46.185(67)	0.177	0.332	47.229(75)	0.669(5)	45.860(78)	0.331	0.744	45.805(51)	1.126	
73(5)	47.174(48)	1.0126(7)	0.713(42)	46.213(89)	0.287	0.385	46.964(76)	0.567(20)	45.921(62)	0.433	0.604	45.135(41)	1.333	
70(5)	47.046(82)	0.9932(18)	0.352(47)	46.125(14)	0.648	0.264	46.231(40)	0.251(95)	46.642(95)	0.749	0.414	46.319(13)	0.689	
67(5)							46.544(1)	0.164(7)	46.650(60)	0.836	0.322	46.159(7)	0.372	

Tab. S4 | Summary of results for the fcc and bcc phases of Fe. Energies (E) and volumes (V) are normalized to one Fe atom. Energy refers to either electronic energy (static) or Gibbs energy (0–300 K). K is the bulk modulus and K' its pressure derivative. μ is the magnetic moment. The final 300 K corrected LDA and GGA values are in bold font.

		E (eV)	V (\AA^3)	K (GPa)	K'	μ
LDA (CA) static	fcc	-9.27578	9.65	341	4.70	0.00
	bcc	-9.17854	10.43	254	4.39	1.95
LDA (CA) 0 K	fcc	-9.25714	9.64	343	4.69	0.00
	bcc	-9.24214	10.48	250	4.41	1.96
LDA (CA) 300 K	fcc	-9.34615	9.69	335	4.71	0.00
	bcc	-9.42047	10.62	236	4.44	1.97
GGA (PBE) static	bcc	-8.45640	11.45	196	4.57	2.21
GGA (PBE) 300 K	bcc	-8.72064	11.69	176	4.32	2.23
Experiment	bcc		11.70	164	5.29	2.20

Tab. S5 | Summary of results for the fcc and bcc phases of Fe. Energies (E) and volumes (V) are normalized to one Fe atom. Energy refers to either electronic energy (static) or Gibbs energy (0–300 K). K is the bulk modulus and K' is its pressure derivative.

		E (eV)	V (\AA^3)	K (GPa)	K'
bcc-Fe	static	-8.4564	11.45	196	4.57
bcc-Fe	300 K	-8.7206	11.68	176	4.32
FM-FeH ^T	static	-11.7051	14.70	169	3.40
FM-FeH ^T	300 K	-11.4352	14.31	192	3.57
FM-FeH ^O -LP	static	-11.8170	13.38	174	4.40
FM-FeH ^O -LP	300 K	-12.0561	13.64	165	3.01

SM46 **References**

- SM47 1. Söderlind, P., Moriarty, J. A. & Wills, J. M. First-principles theory of iron up to earth-core
SM48 pressures: Structural, vibrational, and elastic properties. *Physical Review B* **53**, 14063 (1996).
- SM49 2. Togo, A. & Tanaka, I. First principles phonon calculations in materials science. *Scripta*
SM50 *Materialia* **108**, 1–5 (2015).
- SM51 3. Wallace, D. C. Thermodynamics of crystals. *American Journal of Physics* **40**, 1718–1719
SM52 (1972).
- SM53 4. Sha, X. & Cohen, R. First-principles thermoelasticity of bcc iron under pressure. *Physical*
SM54 *Review B* **74**, 214111 (2006).
- SM55 5. Abdellaoui, M. *et al.* The hydrogen storage properties of mg-intermetallic-hydrides by ab initio
SM56 calculations and kinetic monte carlo simulations. *international journal of hydrogen energy* **45**,
SM57 11158–11166 (2020).

Figures

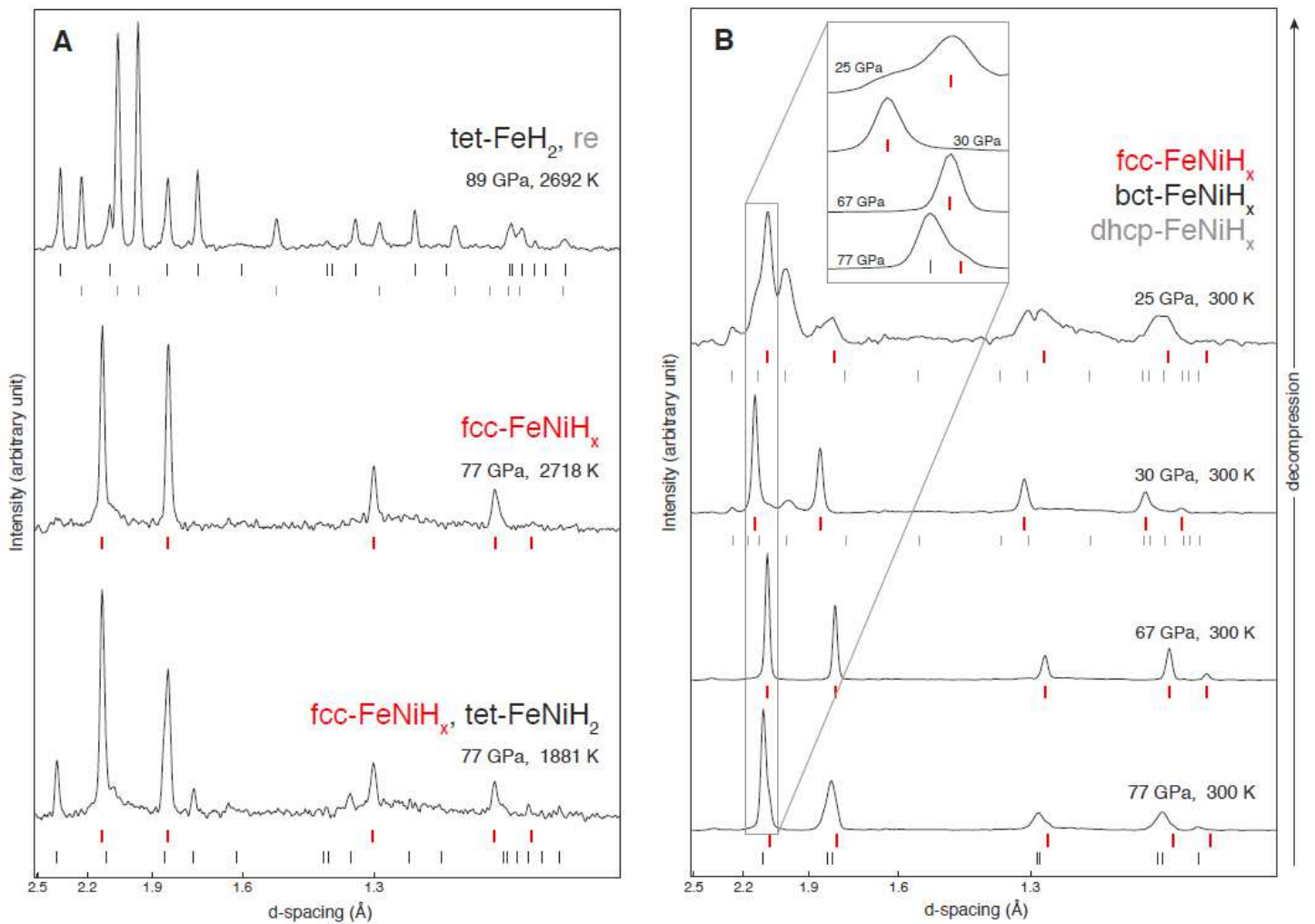


Figure 1

X-ray diffraction for fcc-FeH_x and fcc-FeNiH_x . (A) Patterns measured during heating: bottom for the stability of tet-FeNiH_2 and fcc-FeNiH_x (red ticks) at 77 GPa and 1881 ± 150 K; middle for the full conversion from tet-FeNiH_2 (tetragonal, $I4=mmm$, phase) to fcc-FeNiH_x at 77 GPa and 2718 ± 150 K; and top for stability of tet-FeH_2 (black ticks) at 89 GPa and 2692 ± 150 K. (B) Patterns measured at high pressures and 300 K. The d-spacings of the fcc-FeNiH_x peak anomalously decreases from 77 GPa to 67 GPa, followed by a “normal” gradual increase in d-spacing from 67 to 30 GPa and an abrupt shift to a lower d-spacing at 30 GPa. The d-spacings of the fcc-FeNiH_x experiences an abrupt shift to a lower d-spacing at 25–30 GPa. Below 25 GPa, the peak shifts show expected behavior until the phase converts to bcc-Fe by H loss upon quenching to 1 bar. The inset shows shifts of the 111fcc and 101bct peaks. X-ray diffraction wavelength was 0.3344 \AA .

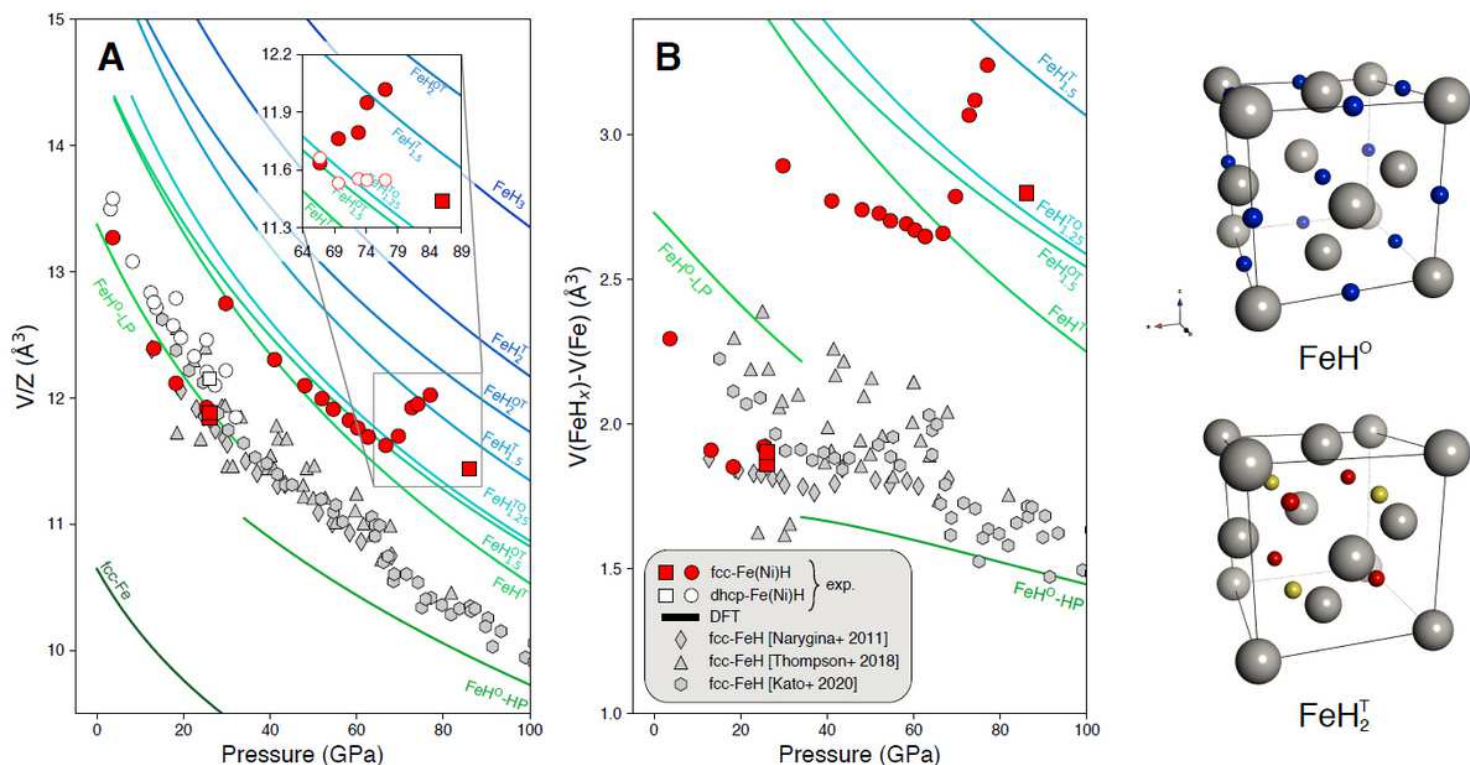


Figure 2

Estimate of H contents in the synthesized fcc phases. Squares represent fcc-FeH_x phases and circles represent fcc-FeNiH_x phases. The red and white colors represent fcc and dhcp phases from this study, respectively, and the colored curves are obtained from our DFT calculations. (A) Unit-cell volume comparison. The inset shows the unit-cell volumes measured above 70 GPa where peak broadening observed for fcc-FeNiH_x can be explained by the two phase model: bct (solid red) + fcc (open red) (see text for details). (B) Unit-cell volume expansion by hydrogen incorporation. We also include data points for FeH_x from previous studies^{6,10,12}. The right panel shows the crystal structures of FeH⁰ and FeH₂^T. The red spheres in FeH₂^T highlight the arrangement of H atoms in a tetrahedral motif which is considered for partial occupancy of H atoms in FeHT.

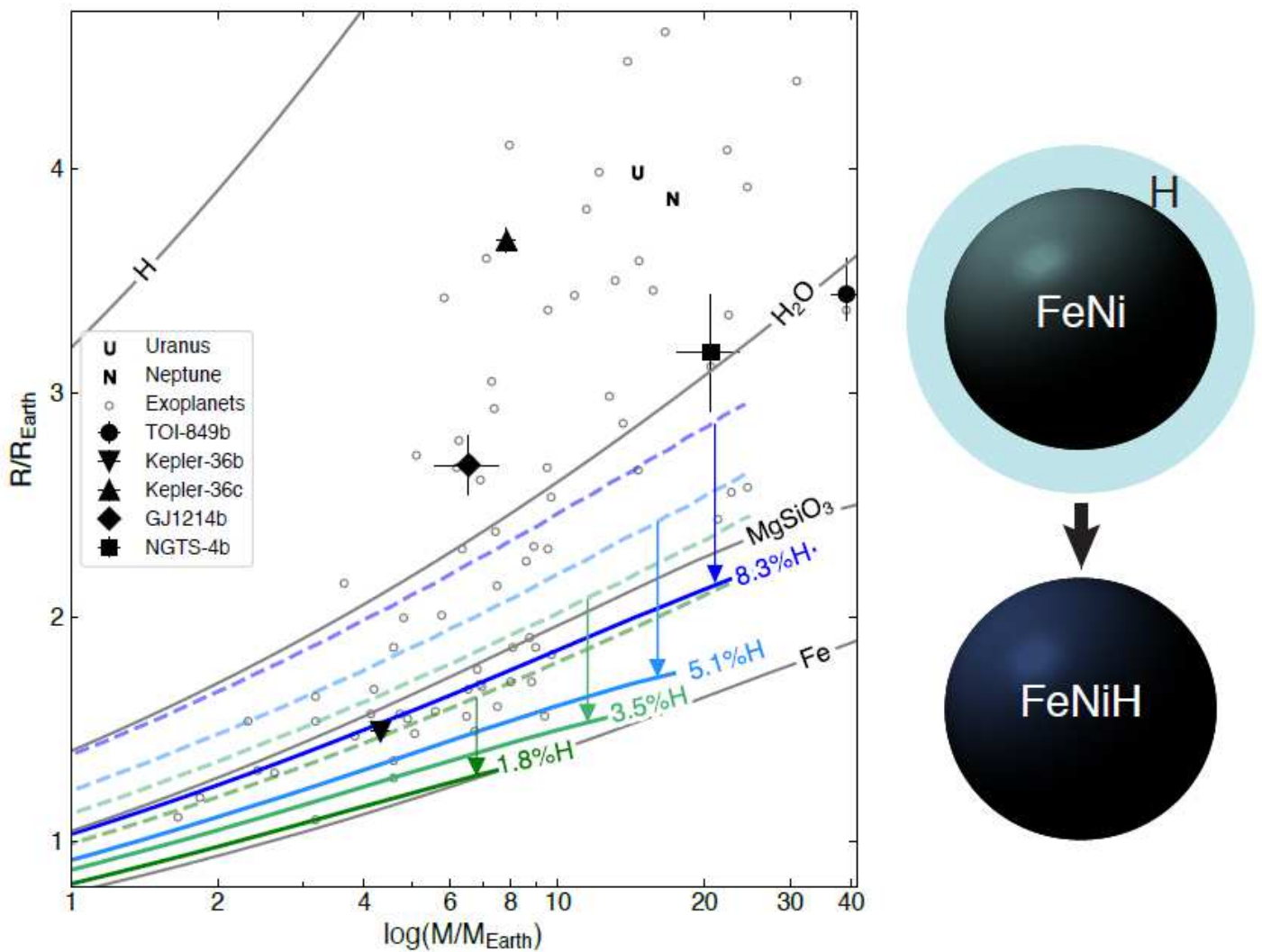


Figure 3

Mass-radius relations of hydrogen-storing metal iron cores (the dark colored curves with varying amount of H in wt%). The light colored curves are the mass-radius relations of pure metallic iron with a separate outer envelope of hydrogen for the same amounts of H. The vertical arrows show the radius decrease by storing H in the core for the same bulk compositions (green, teal, light blue, and blue for H/Fe = 1, 2, 3, and 5, respectively). For comparison, the mass-radius relations for metallic iron (Fe), bridgmanite (MgSiO_3), ice (H_2O), and hydrogen (H) are shown. They are calculated for 300 K. The plot includes the mass and radius of some exoplanets. The gray circles are for exoplanets from NASA exoplanet archive with uncertainties less than 20%.